AIAA JOURNAL
Vol. 40, No. 12, December 2002

# Mechanism of Dynamic Instability of a Reentry Capsule at Transonic Speeds

Susumu Teramoto* and Kozo Fujii†
*Institute of Space and Astronautical Science, Kanagawa 229-8510, Japan*

**A blunt and short reentry capsule tends to be dynamically unstable at transonic speeds, attributed primarily to the delay of base pressure. In the present study the flowfield around a capsule under forced pitching oscillation is numerically simulated, and the results are compared with that around the capsule at a fixed pitch angle. The two flowfields are found to be essentially the same except for a delay in the base pressure in the oscillating case. Detailed flow analysis reveals that impingement of reverse flow behind the capsule determines the base pressure distribution, and the behavior of the reverse flow is governed by the vortex structure behind the capsule. The vortex structure is composed of a ring vortex and a pair of longitudinal vortices, and the interaction between the longitudinal vortices and the flowfield near the neck point defines the flowfield behind the capsule. When the pitch angle is changed, the base pressure does not change until the disturbance of the longitudinal vortices caused by the pitching motion reaches the neck point. This time lag is the cause of the delay of the base pressure. This mechanism reasonably explains the characteristic features observed in the numerical simulation and supports several important features reported in previous experiments.**

## Nomenclature

| | | |
|---|---|---|
| $C_m$ | = | pitch-moment coefficient |
| $C_{mq} + C_{m\dot{\alpha}}$ | = | pitch-damping coefficient |
| $c$ | = | speed of sound |
| $D$ | = | diameter of capsule |
| $f$ | = | frequency |
| $M$ | = | Mach number or pitch moment |
| $p$ | = | static pressure |
| $q$ | = | angular velocity |
| $Re$ | = | Reynolds number |
| $Sr$ | = | Strouhal number |
| $t$ | = | time |
| $u$, $v$, $w$ | = | velocity components |
| $\alpha$ | = | angle of attack |
| $\delta$ | = | delay time |
| $\theta$ | = | pitch angle |
| $\rho$ | = | density |

*Subscripts*

| | | |
|---|---|---|
| $b$ | = | base |
| $f$ | = | front |
| $\infty$ | = | freestream |

## Introduction

SAMPLE-RETURN projects, missions designed for the collection and return of sample from other planets, have recently attracted increased attention. The Institute of Space and Astronautical Science (ISAS) began work on the asteroid sample-return project "Muses-C" in 1995 (Ref. 1) aiming at a launch in 2002 and rendezvous with the asteroid "1998SF36" in 2005. The collected sample will be returned by a reentry capsule that separates from the mother spacecraft in 2007. The sample is expected to produce new knowledge concerning the origin and evolution of the solar system and is of significant scientific interest. It is also a challenging concept from an engineering viewpoint to design a spacecraft that meets the requirements of the mission.

One of the key issues in the design of the spacecraft is the tradeoff between its weight and the reentry velocity. As the weight of the spacecraft is strictly limited, direct reentry is often chosen to eliminate the propellant required for the final deceleration before reentry. As the reentry velocity of such a vehicle is much higher than that from the earth's orbit, heat protection is the most important issue in the design of the sample return capsule. In general, lowering the mass-to-drag ratio reduces the maximum convective heating rate, and a blunt and short capsule that has low mass-to-drag ratio is often adopted for the reentry vehicle of sample-return missions. However, such capsules tend to be dynamically unstable and sometimes enter self-excited oscillation at transonic speeds. These factors also needs to considered in the design of sample-return missions.

This type of dynamic instability has been known and studied since the 1960s,[2–6] yet the detailed mechanism remains largely unknown. The interesting feature of this instability phenomenon is that the reduced frequency defined by the body diameter and the uniform flow velocity is as low as $\mathcal{O}$ (0.01). This experimental result, along with the fact that the instability only occurs at transonic speeds, indicates that high-frequency perturbations such as unsteadiness caused by vortex shedding from the edge of the capsule are not the primary sources of the instability. Recently, Hiraki et al.[7] studied the phenomena experimentally using a one-dimensional free oscillation method and revealed that the dynamic instability is caused by a delay of the base pressure of the capsule. After Hiraki's experiment the present authors numerically studied the flowfield around the capsule in forced pitching oscillation[8] and confirmed that the dynamic instability is caused by the phase delay of the base pressure. The authors also found that the base pressure and the flowfield downstream of the recompression shock wave oscillate with the same delay time. These results indicate that the feedback loop between the capsule, the wake downstream, the flowfield immediately behind the capsule, and the base pressure are the causes of the delay.

The objective of the current study is to reveal the detailed flow mechanism that causes the delay of the base pressure and the cause of the dynamic instability. As it is difficult to discuss the complicated unsteady flowfield directly, the mechanism of the dynamic instability is discussed based on a step-by-step approach. The characteristics of the flowfields around an oscillating capsule are compared with those around the capsule at fixed pitch angles, and a

Received 24 July 2001; revision received 17 July 2002; accepted for publication 25 July 2002. 

*Research Associate, High-Speed Aerodynamics, Yoshinodai 3-1-1, Sagamihara; currently Lecturer, Department of Aeronautics and Astronautics, University of Tokyo, 7-3-1 Hongo, Bunkyo-ku, Tokyo 113-8656, Japan; teramoto@thermo.t.u-tokyo.ac.jp. Member AIAA.

†Professor, High-Speed Aerodynamics, Yoshinodai 3-1-1, Sagamihara. Associate Fellow AIAA.

new flow model is proposed based on the observations. Using this model, the flowfield for the oscillating capsule is discussed based on that for the capsule at fixed pitch angle, and the correlation between the flowfield and the base pressure is discussed in detail. Finally, the mechanism of the dynamic instability is discussed based on the proposed model.

## Numerical Method

The governing equations employed here are the Reynolds-averaged unsteady three-dimensional thin-layer Navier–Stokes equations:

$$\partial_t \hat{Q} + \partial_\xi \hat{E} + \partial_\eta \hat{F} + \partial_\zeta \hat{G} = \partial_\zeta \hat{S}_V$$

Length, density, and velocity are normalized by the diameter of the capsule and the density and speed of sound of the uniform flow, respectively.

Numerical fluxes for the convective terms are evaluated by the simple high-resolution upwind scheme (SHUS),[9] and it is extended to higher order by the MUSCL interpolation based on the primitive variables. The lower–upper alternating directional implicit (LU-ADI) factorized implicit algorithm[10] is employed for time integration. Experience has shown that the LU-ADI scheme has sufficient temporal accuracy to resolve the behavior of large-scale vortex structures provided that the local Courant–Friedrichs–Lewy number is smaller than unity outside the boundary layer. The grid spacing and the time step are carefully chosen in the present study so as to maintain sufficient temporal accuracy to resolve the temporal behavior of the flowfield. The flowfield is considered to be fully turbulent, and Baldwin–Lomax's algebraic turbulence model[11] is applied near the solid wall.

The computational code is based on the authors' in-house code, which has been applied for many compressible flowfields including vortical flow,[12] unsteady flow,[13] and transonic flow.[14] Discussions on the detail and accuracy of the computational code are given in the references.

The capsules examined in the current study are the same as those used in Hiraki's experiment. The forebody is composed of a blunt cone with a spherical nose, and the afterbody is a truncated cone with a flat base. The geometric parameters of the capsules are listed in Table 1, and the D45 model capsule is shown in Fig. 1. The wind-tunnel experiment revealed that the D45 model is dynamically unstable at a small angle of attack and it enters self-excited oscillation at transonic speeds, whereas the D30 model is dynamically stable at all speeds between $M = 0.3 \sim 2.5$.

The computational grid used in the simulation is $151 \times 64 \times 121$ with O-O topology. The minimum grid spacing near the wall is $2.0 \times 10^{-5}$, and the wall coordinate $y^+$ at the first grid point is less than two for the most part of the capsule surface such that at least one grid point is distributed inside the laminar sublayer. The computational domain is $-4.0$ to 10.0 in the $x$ direction and $-10.0$ to 10.0 in the $y$ and $z$ directions. The entire grid system oscillates around the center of gravity of the capsule for the simulation of the flowfield around the oscillating capsule. A grid sensitivity study[8] showed that a coarser $121 \times 64 \times 81$ grid is sufficiently fine to resolve the unsteady behavior of the flowfield behind the capsule. However, a finer grid is used in the present study to improve the spatial resolution and reveal the detailed flow mechanism.

Table 2 shows the flow conditions, corresponding to those of Hiraki's wind-tunnel experiment.[7] The time step $\Delta t$ for the simulation of the flowfield around the oscillating capsule is 1/150,000 of one oscillation cycle, and that for the capsule at fixed pitch angle is set at 0.001 in units of nondimensional time. For both cases $\Delta t$ is approximately $3.4 \times 10^{-7}$ s in physical time. The numerical results indicate that the highest dominant frequency of the flowfield is approximately 1 kHz, corresponding to the Strouhal number ($Sr = fD/u$) of 0.27. Therefore, $\Delta t = 3.4 \times 10^{-7}$ s is sufficiently small to resolve the unsteady fluctuation of the flowfield.

**Table 1 Geometry of model capsules**

| Parameter | D45 model/ D30 model |
|---|---|
| Nose radius | 50 mm |
| Semiapex angle | 45/30 deg |
| Maximum diameter | 100 mm |
| Body length | 50 mm |
| Base configuration | 45-deg truncated cone |
| Dynamic stability at transonic speeds | Unstable/stable |

**Table 2 Flow conditions**

| Parameter | Value |
|---|---|
| Mach number | 1.3 |
| Diameter of capsule | 0.1 m |
| Reynolds number | $2.5 \times 10^6$ |
| Frequency | 20 Hz |
| Maximum pitch angle | ±20 deg |
| Reduced frequency | 0.03 |

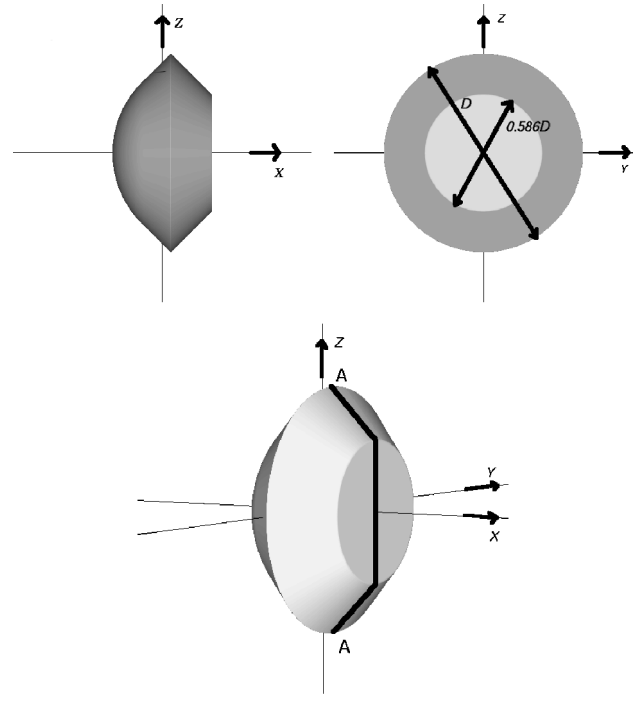


**Fig. 1 D45 model capsule.**

The simulations were carried out on the Fujitsu VPP800/12 at the ISAS. The computation required 20 h on four processing elements (PEs) of VPP800/12 for one forced oscillation cycle. The simulations for the fixed pitch angle were carried out on a single PE, and each case required approximately 30 h.

## Postprocessing

Figure 2 shows the time history of the base pressure of the D45 model fixed at $\alpha = 10$ deg. High-frequency fluctuation of approximately 1 kHz is observed with amplitude reaching 10% of the average pressure. This high-frequency fluctuation is also observed in the simulation of forced pitching oscillation (Fig. 3) and is considered to represent the shedding of small vortices from the edge of the capsule.

As the timescale of the vortex shedding (1 kHz) is very different from that of the oscillation of the capsule (20 Hz), the low-frequency oscillation of the capsule does not appear to be related to the high-frequency shedding of small vortices. The behavior of the small vortices is therefore expected to be the same for both the capsule fixed at a certain pitch angle and the oscillating capsule. The difference between the flowfield around the fixed capsule and the oscillating capsule is the primary concern in the current study, and therefore the influence of the high-frequency component will be excluded in the analysis.

For simulation of the cases with fixed pitch angle, the physical properties are averaged over 20,000 steps (approximately 7 ms in the real time units, sufficient to exclude the disturbance at 1 kHz) after

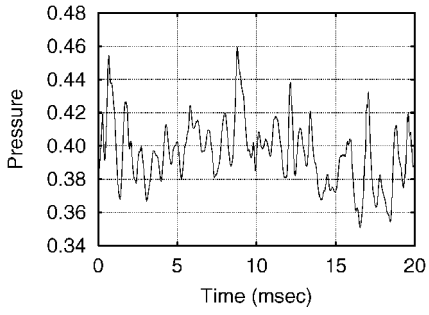


**Fig. 2 Time history of base pressure of D45 model fixed at $\alpha = 10$ deg.**

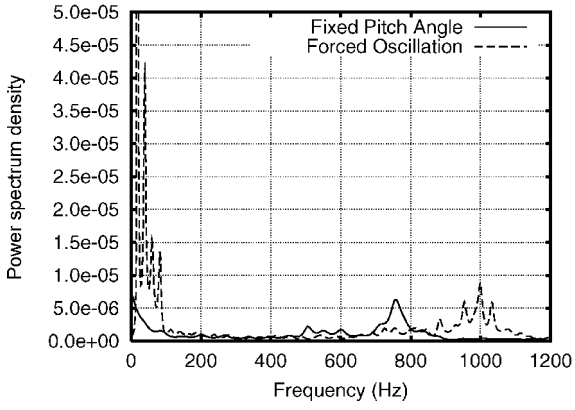


**Fig. 3 Power spectrum density of base pressure.**

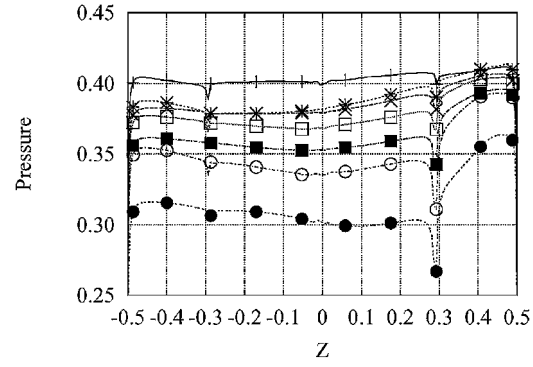


**a) D45 model**

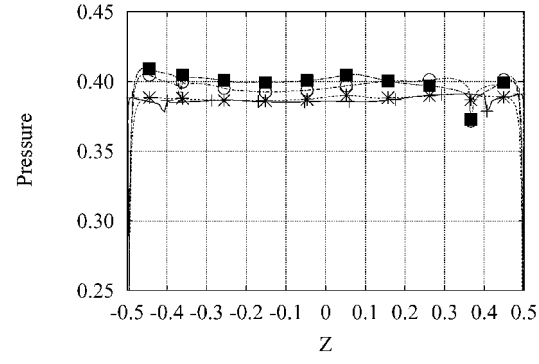


**b) D30 model**

**Fig. 4 Time-averaged base pressure for fixed pitch angle: +, 0 deg; ×, 2.5 deg; ∗, 5.0 deg; □, 7.5 deg; ■, 10 deg; ○, 15 deg; and ●, 20 deg.**

the flowfield has reached the stationary state, and the time-averaged properties are used for discussion. The physical properties obtained from the unsteady simulation of the forced oscillation are processed by a low-pass filter (LPF) with a cutoff frequency of 150 Hz in order to eliminate the high-frequency fluctuation. The dominant frequency of the flowfield is 20 Hz, which is sufficiently low compared to the cutoff frequency to avoid distortion of the fundamental behavior of the flowfield by the LPF. The details and usefulness of this filtering method are described in Ref. 15.

## Results and Discussion

### Aerodynamic Forces and Base Pressure

The characteristics of the base pressure and the aerodynamic pitching moment caused by the base pressure are discussed first.

*Time-Averaged Base Pressure Distributions for Capsule at Fixed Pitch Angle*

The time-averaged base pressure distributions along the centerline (line A-A in Fig. 1) are plotted against the $z$ coordinate for several fixed pitch angles in Fig. 4. The base pressure of the D45 model (Fig. 4a) decreases uniformly in the region $z < 0.3$ (lower side of the base) as the angle of attack increases. The pressure at $z > 0.3$ also decreases but to a lesser degree. The pressure difference between $z < 0.3$ and $z > 0.3$ increases as the angle of attack increases. On the other hand, the base pressure of the D30 model is almost uniform, even when the pitch angle is positive (Fig. 4b).

The difference in the base pressure distributions can be discussed more clearly using the aerodynamic pitching moment. The overall aerodynamic pitching moment as a result of the surface pressure acting on the capsule is given by $M = \oint p\boldsymbol{n} \times \boldsymbol{r} \cdot \mathrm{d}s$. Here, the contributions from the front pressure and base pressure are discussed separately to account for considerable difference between the flowfields at the front and back of the capsule. The total pitching moment is therefore given by

$$M = M_f + M_b \tag{1}$$

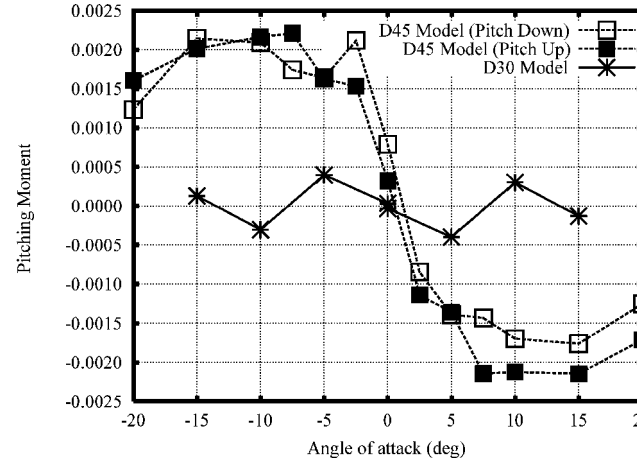


**Fig. 5 Base pitching moment of D45 and D30 models (fixed pitch angle).**

where $M_f$ and $M_b$ are the pitching moments of the front and base, expressed as

$$\begin{cases} M_f(\alpha) = \oint_{\text{front area}} p\boldsymbol{n} \times \boldsymbol{r} \cdot \mathrm{d}s \\ M_b(\alpha) = \oint_{\text{base area}} p\boldsymbol{n} \times \boldsymbol{r} \cdot \mathrm{d}s \end{cases} \tag{2}$$

Figure 5 shows the variation in $M_b$ with pitch angle. Two curves, one for when the capsule quasistatically pitches up and another for when it quasistatically pitches down, are shown for the D45 model. Here, "quasistatic" means that a converged solution at a certain (fixed) pitch angle is used as the initial flowfield for simulation at the next pitch angle.

The base pitching moment of the D45 model is positive (pitch up) for negative pitch angles and negative for positive pitch angles. The base pressure distributions shown in Fig. 4a indicate that the

high-pressure region at $z > 0.3$ (upper side of the base) is the origin of the pitch-down moment. The two curves for the D45 model coincide, and there is no sign of static hysteresis.

The base pitching moment of the D30 model is almost flat, which is consistent with the uniform pressure distributions shown in Fig. 4b.

*Evaluation of Dynamic Characteristics Based on Static Base Pressure Distributions*

Suppose that the surface pressure of the capsule oscillates with a delay time $\delta$ with respect to the pitch angle. (Hereafter, this assumption is named "constant-delay model.") Considering a capsule oscillating in pitch with $\alpha = \alpha_{\max} \sin(\omega t)$, the aerodynamic pitching moment acting on the capsule during the oscillation can be described as

$$M_{f_{\text{delay}}}(t) = M_{f_{\text{fixed}}}\{\alpha_{\max} \sin[\omega(t - \delta_f)]\} \tag{3}$$

$$M_{b_{\text{delay}}}(t) = M_{b_{\text{fixed}}}\{\alpha_{\max} \sin[\omega(t - \delta_b)]\} \tag{4}$$

where the subscript "fixed" denotes the moment that acts on the capsule at a fixed pitch angle and "delay" denotes the constant-delay model. Here, $M_{b_{\text{fixed}}}$ depends only on the pitch angle because there is no static hysteresis. The result of the forced-oscillation simulation[8] showed that $\delta_f \simeq 0$ and $\omega\delta_b \ll 1$, then

$$M_{(t)} = M_{f_{\text{delay}}}(t) + M_{b_{\text{delay}}}(t)$$

$$= \left[M_{f_{\text{fixed}(\alpha)}} + M_{b_{\text{fixed}(\alpha)}}\right] - \delta_b \left.\frac{\partial M_{b_{\text{fixed}}}}{\partial \alpha}\right|_{\alpha} \dot{\alpha} + \mathcal{O}(\alpha^2) \tag{5}$$

The aerodynamic pitching moment acting on the object in a uniform flow is expressed using the aerodynamic coefficients as follows:

$$M = \tfrac{1}{2}\rho_\infty u_\infty^2 SD \cdot [C_m + (C_{\text{mq}} + C_{m\dot{\alpha}})(D/u_\infty)\dot{\theta}] \tag{6}$$

Note that $\theta = \alpha$ because the object is placed in the uniform flow. Comparing Eqs. (5) and (6), the following relations are obtained:

$$C_m \propto M_{f_{\text{fixed}}}(\alpha) + M_{b_{\text{fixed}}}(\alpha) \tag{7}$$

$$C_{\text{mq}} + C_{m\dot{\alpha}} \propto -\delta_b \left.\frac{\partial M_{b_{\text{fixed}}}}{\partial \alpha}\right|_{\alpha} \tag{8}$$

Because $M_f$ is much larger than $M_b$, Eqs. (7) and (8) indicate that the static aerodynamic characteristic of the capsule depends mainly on $M_f$, whereas the dynamic characteristic is mainly determined by the gradient of $M_b$. Both Hiraki's experiment[7] and the authors' numerical study[8] showed that the dynamic instability of the capsule is caused by the delay of the base pressure. These results support the observation derived from Eq. (8).

The gradient of $M_b$ can be directly evaluated from the simulations of the flowfield around the capsule at fixed pitch angles. The dynamic characteristic of the capsule can then be determined without the simulation of forced oscillation provided that the base pitching moment $M_b$ during the forced oscillation can be approximated by the constant-delay model.

*Comparison with Simulation Results for Forced Oscillation*

The base pitching moment of the D45 model shown in Fig. 5 can be approximated by a function of $\alpha$ as follows:

$$M_{b_{\text{fixed}}}(\alpha) = \begin{cases} a_M \tanh(b_M \alpha) & |\alpha| < \alpha_{M0} \\ c_M(\alpha - \alpha_{M0}) + a_M \tanh(b_M \alpha_{M0}) & \alpha > \alpha_{M0} \\ c_M(\alpha + \alpha_{M0}) - a_M \tanh(b_M \alpha_{M0}) & \alpha < -\alpha_{M0} \end{cases} \tag{9}$$

$$c_M = a_M b_M \left[1 - \tanh^2(b_M \alpha_{M0})\right]$$

$$a_M = -0.0019, \qquad b_M = 0.5, \qquad \alpha_{M0} = 5.5$$

Substituting Eq. (9) into Eq. (4), the pitch moments $M_{b_{\text{delay}}}$ are plotted for several values of $\delta_b$ in Fig. 6. The curves show the time

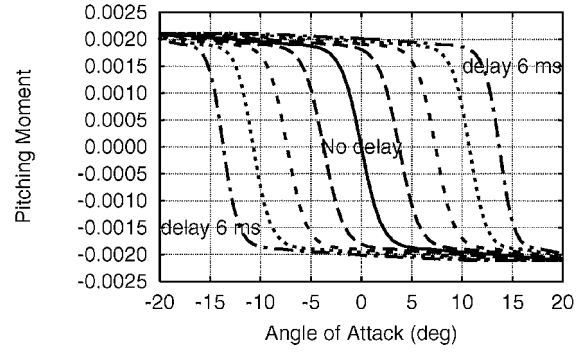


**Fig. 6 Base pitching moment of D45 model (constant-delay model): ——, no delay; — —, delay 1.5 ms; – – -, delay 3.0 ms; - - - - -, delay 4.5 ms; and — - -, delay 6.0 ms.**

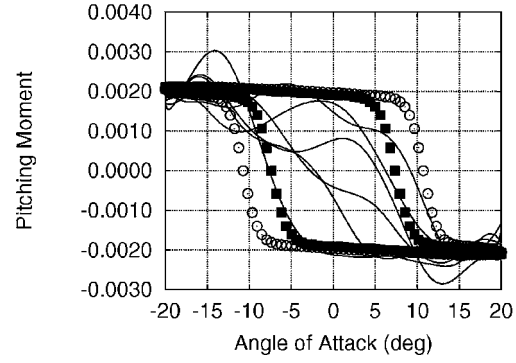


**Fig. 7 Base pitching moment of D45 model (forced oscillation): ——, forced oscillation; ■, fixed pitch + delay 3.0 ms; ○, fixed pitch + delay 4.5 ms.**

histories of $M_{b_{\text{delay}}}$ evaluated by the constant-delay model for delay times of 1.5, 3.0, 4.5, and 6.0 ms. The solid curve in Fig. 7 shows the actual history of the base pitching moment $M_b$ for the D45 model capsule in forced pitching oscillation. The histories of $M_{b_{\text{delay}}}$ evaluated from the constant-delay model are plotted as symbols in the figure. The magnitude of $M_b$ remains almost constant at $\pm 0.002$ up to a certain angle of attack, at which $M_b$ reverses in sign. The $M_b$ curves are close to the plots of the simple constant-delay model for a delay time of roughly $\delta = 3.0$ ms, although the delay time is scattered between cycles.

The base pitching moment during the forced oscillation is reasonably approximated by the simple constant-delay model. The characteristic of the base pressure distribution reflects the behavior of the flowfield behind the capsule, and therefore the agreement of $M_b$ indicates that the flowfield behind the oscillating capsule can also be expressed by the constant-delay model. That is, the mechanism of the flowfield that determines the base pressure distribution of the oscillating capsule is essentially the same as that for the capsule at a fixed pitch angle with the delay time in mind. Therefore, it is possible to discuss the correlation between the flow structure and the dynamic stability of the capsule from the simulation of the flowfield around the capsule at a fixed pitch angle.

**Unsteady Base Pressure Distributions for Capsule at Fixed Pitch Angle**

The base pressure distributions for the D45 model (dynamically unstable) and D30 model (dynamically stable) fixed at $\alpha = 10$ deg are discussed in detail in this section.

Time histories of the base pressure at four points on the base (locations shown in Fig. 8) for the two capsules are shown in Figs. 9a and 9b. The time-averaged base pressure for the D45 model at $\alpha = 10$ deg is approximately 0.36 (Fig. 4a), and instantaneous base pressure at the three points (right, bottom, and left) fluctuates within the range of $0.37 \pm 0.01$. The pressures at the point top also fluctuate marginally around 0.38 for the most part but occasionally rise to approximately 0.45. As the base pressure distribution for the D45 model is a superposition of a constant value and intermittent pressure peaks, the time-averaged pressure distribution depends on the behavior of the

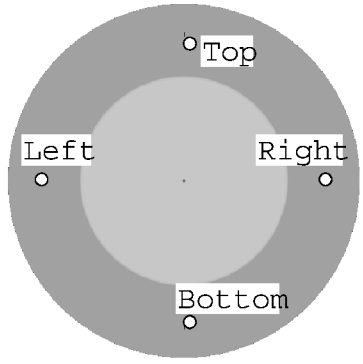


**D45 model**

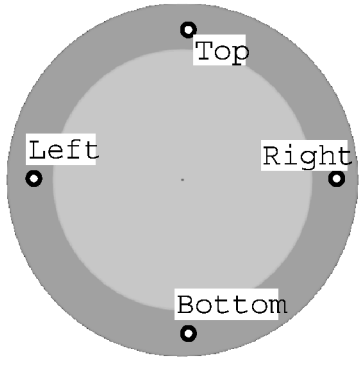


**D30 model**

**Fig. 8 Location of pressure ports.**

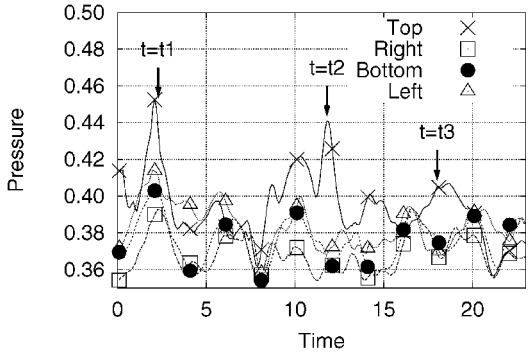


**a) D45 model**

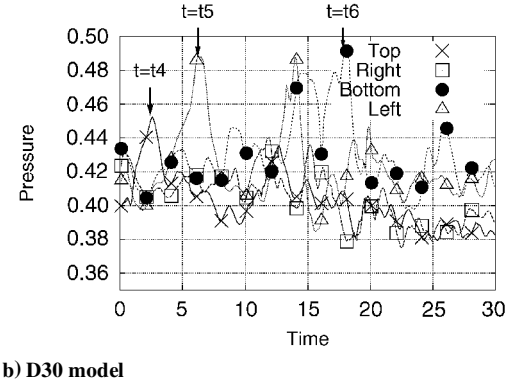


**b) D30 model**

**Fig. 9 Time history of base pressure.**

pressure peaks. The time-averaged pressure at the leeward (upper) side of the D45 model is higher because the pressure peaks appear only in the top region.

The base pressure for the D30 model is also expressed as the superposition of a constant value and intermittent pressure peaks as shown in Fig. 9b. However, in this case the peaks appear randomly over the base, with the result that the time-averaged base pressure of the D30 model is almost uniform.

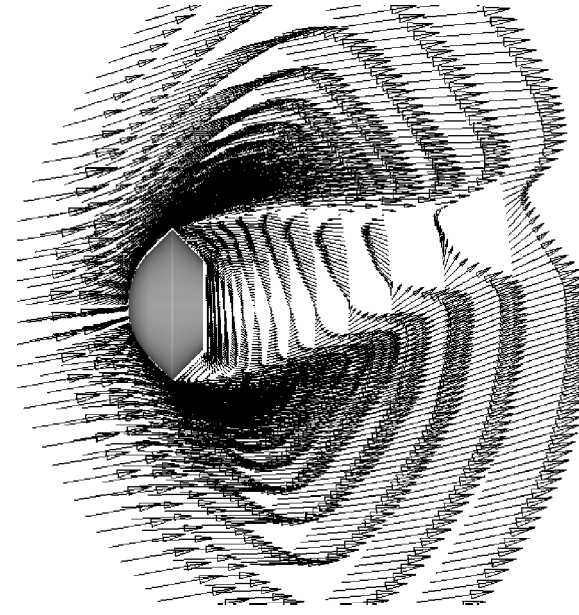

**Fig. 10 Vector map in symmetry plane ($\alpha$ = 10 deg, time averaged).**

The difference in the characteristics of the time-averaged base pressure distribution reflects the difference in the unsteady behavior of the pressure peaks. Therefore, the flow mechanism that causes these pressure peaks is considered to be related to the dynamic instability of the capsule.

### Correlation Between Base Pressure and Velocity Field

Figure 10 shows the time-averaged velocity vectors in the plane of symmetry of the D45 model with pitch fixed at $\alpha = 10$ deg. A reverse flow region is observed behind the capsule with a maximum velocity of $u \simeq -0.5$. The nondimensional density inside the recirculating region is $\rho \simeq 0.4$, and the resulting nondimensional dynamic pressure is $\frac{1}{2}\rho u^2 \simeq 0.05$, which is consistent with the height of the pressure peaks in Figs. 9a and 9b.

Figures 11 and 12 show the correlation between the reverse flow and the base pressure. The figures correspond to the instances when the pressure peaks, indicated by the arrows $t1 \sim t6$ in Fig. 9, appear on the base. The semitransparent surface is the isosurface of axial velocity $u = -0.4$, representing the core region of the reverse flow. The shading of the capsule denotes the static pressure distribution. The contours of axial velocity are plotted on three planes: $x = 1.0$, 1.5, and 2.0. The contours are displayed only for the subsonic region, and therefore the shapes of the contour planes represent the cross sections of the wake on each plane.

The high-pressure regions at the base (light area) always appear at the head of the reverse flow. For the D45 model (Fig. 11) the reverse flow passes the upper side of the wake, and the high-pressure spot always appears at the point top part of the base. On the other hand, the reverse flow of the D30 model (Fig. 12) passes the upper side when the high-pressure spot appears at the point top ($t = t4$), the left side when the high-pressure spot appears at the point left ($t = t5$), and the lower side when the high-pressure spot appears at the point bottom ($t = t6$). These figures indicate that the high-pressure spots are caused by the impingement of the reverse flow against the base.

The primary difference between the reverse flows of the two capsules is their downstream position. The reverse flow of the D45 model passes the upper side of the wake at all three cross sections, whereas the flowfield behind the D30 model is essentially axisymmetric even for positive pitch angles and the reverse flow passes almost through the center of the wake at sections $x = 1.5$ and 2.0.

### Vortex Structure Behind the Capsule

*Time-Averaged Streamlines*

Figure 13 shows the time-averaged streamlines behind the capsules fixed at a pitch angle $\alpha = 10$ deg. Two-dimensional time-averaged streamlines in the plane of symmetry are shown in Fig. 14.

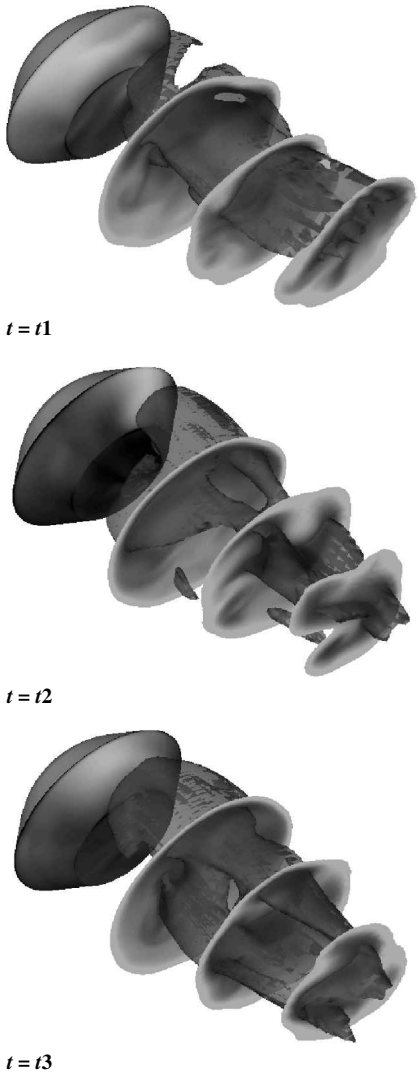


**Fig. 11 Reverse flow and base pressure (D45 model, $\alpha$ = 10 deg).**

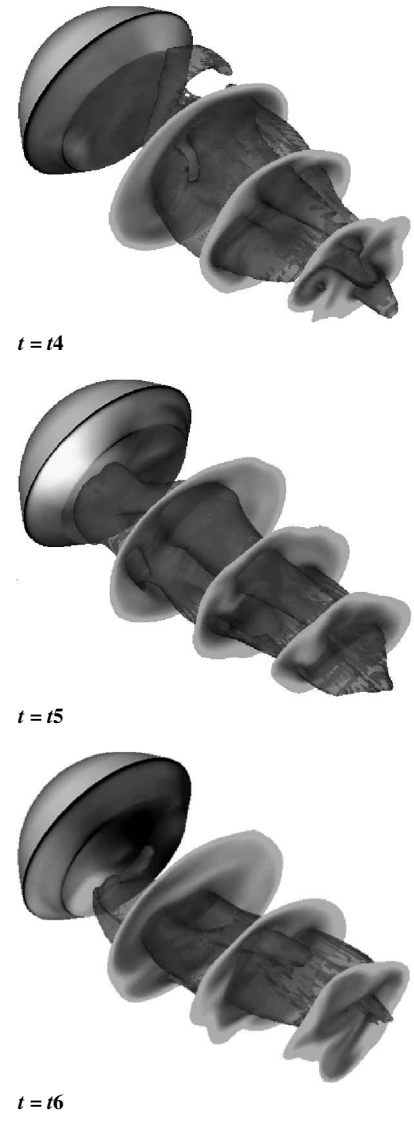


**Fig. 12 Reverse flow and base pressure (D30 model, $\alpha$ = 10 deg).**

A pair of large vortices is observed behind the D45 model (Fig. 13a). The vortices are the counterclockwise vortices observed from the left side (Fig. 14a) and push the reverse flow upward. The streamlines behind the D30 model (Fig. 13b) are distorted almost randomly, and no clear flow structure is observed from the streamlines. In Fig. 14b the upper vortex (clockwise) and lower vortex (counterclockwise) are the same size, and the flowfield behind the D30 model is almost axisymmetric even though the capsule has nonzero pitch angle.

It becomes clear that the flow structure that makes the wake asymmetric and shifts the reverse flow upward is the pair of vortices behind the capsule.

*Vortex Core*

As the three-dimensional structure of the vortices behind the capsule is difficult to recognize in the two-dimensional pictures of the streamlines (for example, Figs. 13), the behavior of the vortices behind the capsule was discussed based on the two-dimensional streamlines in the plane of symmetry (Fig. 14) in the preceding section. The vortex-core identifying technique developed by Sawada[16] is applied here for discussion of the three-dimensional structure of the vortices. The method locates the core of the vortices automatically based on a critical-point analysis and visualizes the vortices as the locus of the vortex core, providing a clearer view of the vortex structure than the streamlines. Figure 15d shows the locus of the vortex core behind the D45 model fixed at $\alpha = 10$ deg. The arrows in the figure denote the direction of propagation of the vortices. Figures 15a–15c show the two-dimensional streamlines inside each cross section.

The vortex behind the capsule is composed of a distorted ring vortex and a pair of longitudinal vortices that emanate from the kink of the ring vortex. The ring vortex corresponds to the reverse flow, as shown in Fig. 15a, and the two contrarotating vortices observed in Fig. 14 are in fact the cross sections of the single ring vortex. The behavior of the reverse flow is correlated with the shape of the ring vortex: when the lower part of the ring vortex is located forward, the reverse flow is directed upward, passes the upper side of the wake, and impinges on upper part of the base.

The vortices in Fig. 15c are a pair of longitudinal vortices. The right vortex rotates clockwise, the left vortex rotates counterclockwise, and both vortices propagate downstream. The vortices in Fig. 15b also appear to be longitudinal vortices, yet they are actually parts of the distorted ring vortex. Although the vortices in Figs. 15b and 15c are separate vortices, both rotate in the same direction and emanate from the neck point at which the shear layer converges. It appears that the vortices in Figs. 15b and 15c are both induced by the flow structure at the neck point.

*Pair of Longitudinal Vortices*

The discussions so far have focused mainly on the flow structure inside the recirculating region. Figure 16 shows a sideview of the streamlines inside the shear layer surrounding the recirculating region. The flow structure inside the shear layer is also shown schematically in Fig. 17.

The flow inside the shear layer is directed upward at the neck point. The upswept flows induce the pair of longitudinal vortices

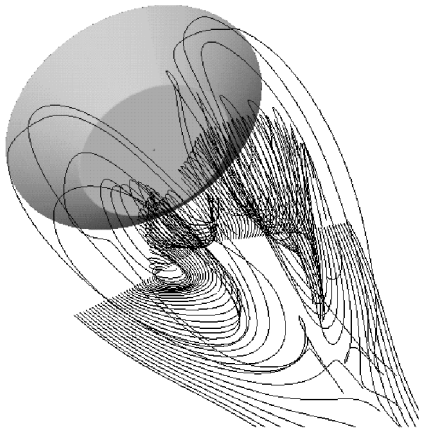

a) D45 model

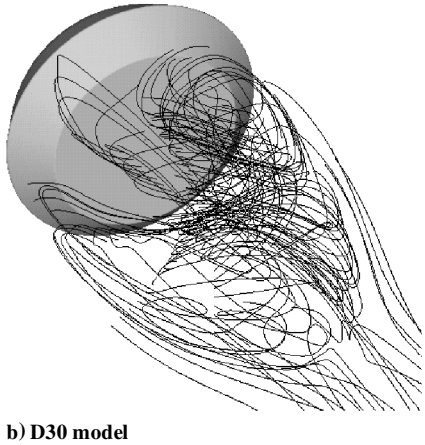

b) D30 model

**Fig. 13 Streamlines behind capsule ($\alpha$ = 10 deg, time averaged).**

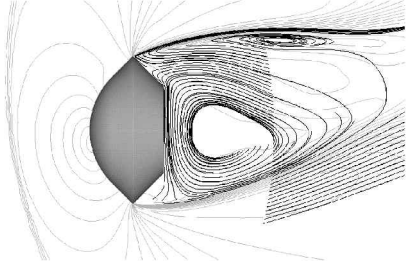

a) D45 model

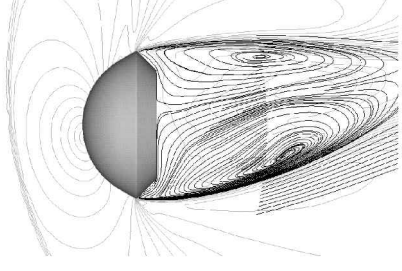

b) D30 model

**Fig. 14 Streamlines in symmetry plane ($\alpha$ = 10 deg, time averaged).**

downstream and also cause the ring vortex inside the recirculating region to deform. These figures show that the upswept flows at the neck point are closely related to the vortex structure discussed in the preceding section.

The upswept streams are formed by the convergence of upstream streamlines. In Fig. 16 the streamlines are directed slightly downward between the capsule and the neck point and converge at the lower part of the neck point, then roll up to form the upswept flows. The direction and convergence of the streamlines between the capsule and the neck point appear to be the key factors determining the flow structure behind the capsule.

## Mechanism of Dynamic Instability

It has been found that the flowfield behind the oscillating capsule can be approximated by the constant-delay model and that the flowfield is governed by the deformed ring vortex and the pair of longitudinal vortices.

Considering that the dynamic instability of the capsule is caused by the delay of the base pressure, the mechanism of the dynamic instability can be summarized as follows.

When the pitch angle of the capsule is changed, the base pressure does not change until the effect of the change in pitch angle reaches the base through the following four steps:

1) The pressure field at the front of the capsule changes immediately when the attitude of the capsule changes. The pressure field rotates the flow inside the shear layer behind the capsule downward, and the disturbance in the direction of the streamline propagates downstream.

2) The streamlines directed downward converge at the rear end of the recirculating region (neck point). The streamlines then roll up and form upswept flows. The formation of the upswept flows near the neck point is delayed slightly with respect to the motion of the capsule because the speed of propagation inside the shear layer is finite.

3) The roll up generates a pair of longitudinal vortices both upstream and downstream. The upstream longitudinal vortices distort the ring vortex behind the capsule and shift the reverse flow upward.

4) The reverse flow impinges on top of the base, and the surface pressure at the upper part of the base becomes higher than the lower part. The change in base pressure distribution gives rise to pitch-down moment.

From these mechanisms we derive $\delta_b > 0$ and $\partial M_{b_{\text{fixed}}}/\partial\alpha|_\alpha < 0$. Equation (8) shows that the capsule is dynamically unstable when $\delta_b(\partial M_{b_{\text{fixed}}}/\partial\alpha)|_\alpha < 0$. Therefore, the capsule is dynamically unstable until a certain pitch angle is reached.

## Numerical Experiments

Under the mechanism described in the preceding section, the delay of the base pressure reflects the propagation of the downward velocity component inside the shear layer from the edge of the capsule to the neck point. The speed of propagation and the distance between the capsule and the neck point are considered to be proportional to the freestream velocity $U_\infty$ and the diameter of the capsule $D$, respectively. Therefore, the delay time $\delta$ is proportional to $D/U$ for a given capsule shape and is independent of the frequency of the pitching oscillation. The phase angle $\phi$ is given by $\phi = 2\pi f\delta$, and the delay phase angle should be proportional to the frequency $f$.

Additional simulations were carried out to verify this hypothesis. The flowfield around the D45 model under the forced pitching oscillation was numerically simulated using the same grid and flow conditions. In this case the frequency of the forced oscillation was set at 40 Hz, which is double that for the preceding simulation.

The characteristic parameters for base pressure oscillation are compared with those for oscillation at 20 Hz in Table 3. The time-averaged pressure and amplitude of the oscillation are almost same for the two frequencies, yet the phase angle for 40 Hz is approximately double that for 20 Hz. The delay phase angle is therefore proportional to the frequency of oscillation, supporting the hypothesis.

**Table 3 Characteristics of base pressure oscillation for different frequencies**

| Frequency, Hz | Average pressure | Amplitude | Phase angle, deg |
|---|---|---|---|
| 20 | 0.3163 | 0.03604 | −16.4 |
| 40 | 0.3141 | 0.03495 | −29.4 |

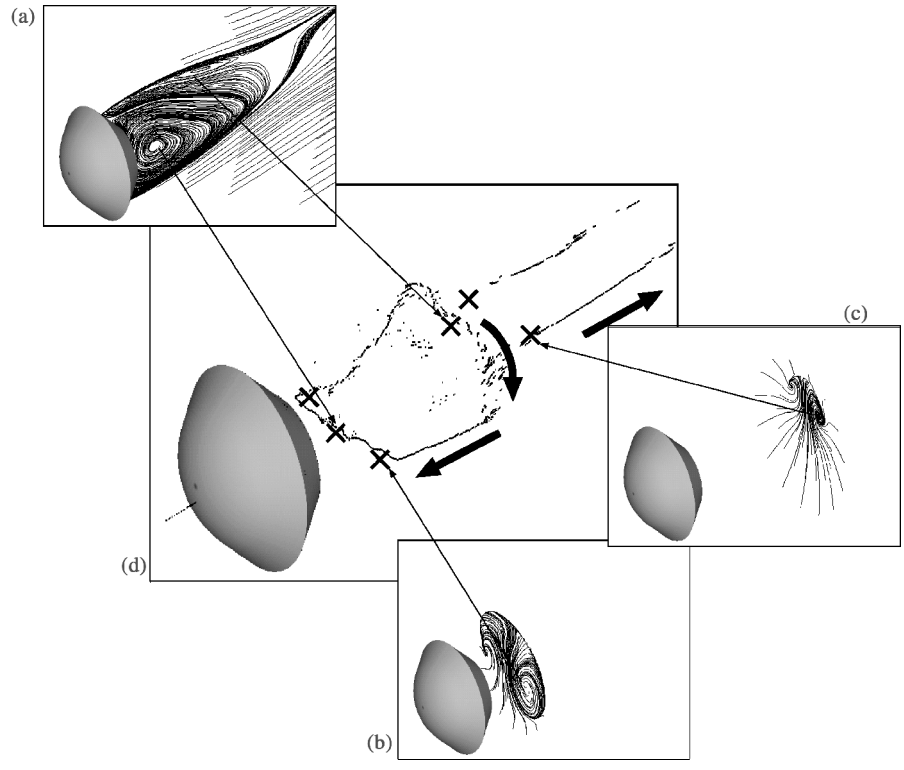


**Fig. 15 Locus of vortex core ($\alpha$ = 10 deg, time averaged).**

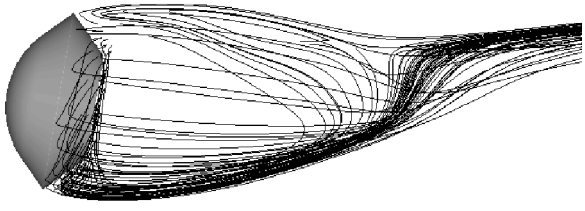

**Fig. 16 Streamlines inside shear layer ($\alpha$ = 10 deg, time averaged).**

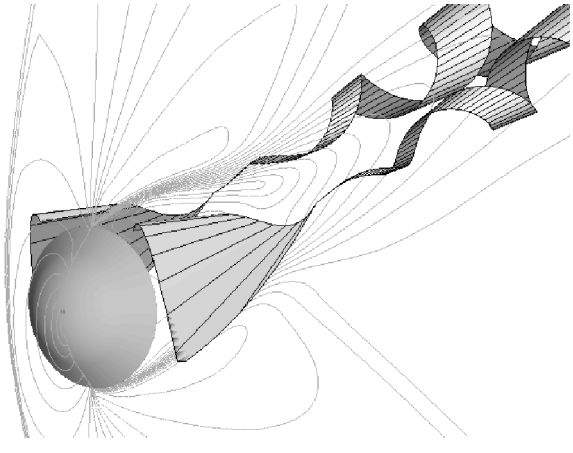

**Fig. 17 Schematic view of longitudinal vortex pair.**

## Conclusions

The flowfields around blunt capsules, which represent the reentry capsule used in sample-return missions, were numerically studied in order to better understand the mechanism of dynamic instability of the capsule at transonic speeds.

The flowfield around the capsule at a fixed angle of attack was compared with that around the capsule under pitching oscillation. The change in the distribution of the surface pressure was essentially the same for the two flowfields except for a slight time delay at the base. The surface pressure of the oscillating capsule was modeled by a simple constant-delay model, and the dynamic stability of the capsule was discussed based on this model. It was shown that the dynamic stability of the capsule depends mainly on the behavior of the base pressure and that the capsule is dynamically unstable when the change in the pitch-down moment induced by the base pressure distribution at positive pitch angle is delayed with respect to the change in the pitch angle.

The characteristics of base pressure were discussed based on a simulation of the flowfield around the capsule at fixed pitch angles. There is strong reverse flow behind the capsule, and the impingement of the reverse flow on the base determines the base pressure distribution. The flowfield behind the capsule is characterized by a vortex composed of a ring vortex and a pair of longitudinal vortices. The longitudinal vortices induce upswept flows at the neck point when the capsule pitches up, the upswept flows push the reverse flow upward, and the change in the base pressure distribution produces a pitch-down moment. The base pressure does not change as a result of the change in pitch angle of the capsule until the change of the longitudinal vortices as a result of the attitude change propagates downstream and reaches the neck point. This time lag causes the phase delay of the base pressure.

The base pressure distribution and delay are closely related to the behavior of the pair of longitudinal vortices, and therefore the dynamic stability of the capsule is considered to be related to the formation of the pair of the longitudinal vortices downstream.

The mechanism of dynamic instability derived in this study reasonably explains the major features observed in the numerical simulations and is consistent with several important features reported in previous experiments.

## References

[1]Working group of Asteroid Sample Return Mission, "Asteroid Exploration Plan (Muses-C)," Inst. of Space and Astronautical Science, Kanagawa, Japan, March 1995 (in Japanese).

[2]Wright, B. R., and Kilgore, R. A., "Aerodynamic Damping and Oscillatory Stability in Pitch and Yaw of Gemini Configurations at Mach Numbers from 0.50 to 4.63," NASA TN D-3334, March 1966.

[3]Sammonds, R. I., and Kruse, R. L., "Viking Entry Vehicle Aerodynamics at $M = 2$ in air and some preliminary test data for flight in $CO_2$ at $M = 11$," NASA TN D-7974, June 1975.

[4]Yoshinaga, T., Tate, A., Watanabe, M., and Shimoda, T., "Orbital Re-Entry Experiment Vehicle Ground and Flight Dynamic Test Results Comparison," *Journal of Spacecraft and Rockets*, Vol. 33, No. 5, 1996, pp. 635–642.

[5]Berner, C., and Winchenbach, G. L., "A Numerical and Experimental Investigation of Generic Space Probes, AIAA Paper 98-0798, Jan, 1998.

[6]Chapman, G. T., and Yates, L. A., "Dynamics of Planetary Probes: Design and Testing Issues," AIAA Paper 98-0797, Jan. 1998.

[7]Hiraki, K., Inatani, Y., Ishii, N., Nakajima, T., and Hinada, M., "Dynamic Stability of MUSES-C Capsule," *21st International Symposium on Space Technology and Science*, edited by K. Uesugi, 21st ISTS Publication Committee, 1998, ISTS 98-d-83.

[8]Teramoto, S., Hiraki, K., and Fujii, K., "Numerical Analysis of Dynamic Stability of a Reentry Capsule at Transonic Speeds," *AIAA Journal*, Vol. 39, No. 4, 2001, pp. 635–642.

[9]Shima, E., and Jounouchi, T., "Role of CFD in Aeronautical Engineering (No. 14)—AUSM Type Upwind Schemes," *Proceedings of the 14th NAL Symposium on Aircraft Computational Aerodynamics*, National Aerospace Lab., NAL SP-34, Tokyo, 1997, pp. 7–12.

[10]Obayashi, S., Matsushima, K., Fujii, K., and Kuwahara, K., "Improvements in Efficiency and Reliability for Navier–Stokes Computations Using the LU-ADI Factorization Algorithm," AIAA Paper 86-0338, Jan. 1986.

[11]Baldwin, B. S., and Lomax, H., "Thin Layer Approximation and Algebraic Model for Turbulent Flows," AIAA Paper 78-257, Jan. 1978.

[12]Fujii, K., and Obayashi, S., "High-Resolution Upwind Scheme for Vortical-Flow Simulation," *Journal of Aircraft*, Vol. 26, No. 12, 1989, pp. 1123–1129.

[13]Ogawa, T., and Fujii, K., "Numerical Investigation of Three-Dimensional Compressible Flows Induced by a Train Moving into a Tunnel," *Computers and Fluids*, Vol. 26, No. 6, 1997, pp. 565–585.

[14]Fujii, K., and Obayashi, S., "Navier–Stokes Simulations of Transonic Flows over a Practical Wing Configuration," *AIAA Journal*, Vol. 25, No. 3, 1987, pp. 369, 370.

[15]Teramoto, S., and Fujii, K., "Preprocessed Visualization of Large Scale Unsteady Flow Simulations," *Journal of Visualization*, Vol. 3, No. 4, 2001, pp. 313–322.

[16]Sawada, K., "A Convenient Visualization Method for Identifying Vortex Cores," *Transactions of the Japan Society of Aeronautical and Space Sciences*, Vol. 38, No. 120, 1995, pp. 102–120.

A. Plotkin
*Associate Editor*